Large-Scale Solar Eruptions

Natchimuthukonar Gopalswamy

Abstract This chapter provides an over view of coronal mass ejections (CMEs) and the associated flares including statistical properties, associated phenomena (solar energetic particles, interplanetary shocks, geomagnetic storms), and their heliospheric consequences.

1 Introduction

A solar eruption can be defined as a transient ejection of material from the solar atmosphere. Transient eruptions occur from closed field regions of all sizes, starting from bright points to large active regions. In this chapter, we consider only those eruptions, which have observable manifestations in white light images obtained by coronagraphs. Coronagraphs are instruments that have an occulting disk that block the bright solar disk so the faint corona can be observed by means of Thomson scattered photospheric light. In coronagraph images, the large-scale eruptions are observed as moving bright features. Usually moving features with an angular width of a few degrees or more are known as coronal mass ejections (CMEs). Solar flares associated with CMEs are known as eruptive flares in contrast to compact flares, which are not associated with any mass motion. Flares represent electromagnetic emission observed prominently in soft X-rays, EUV, and H-alpha. Nonthermal emission is also observed over the entire radio spectrum (from kilometric to millimetric wavelengths), hard X-rays, and gamma rays. Flares cause enhanced ionization in the terrestrial ionosphere causing sudden ionospheric disturbances (SIDs) that seriously affect radio communication and navigation (Davies 1990). Energetic particles accelerated in flares and CME-driven shocks can be potentially harmful to space technology and humans in space. Energetic CMEs propagate far into the heliosphere causing observable effects along their path, sometimes all the way to the

N. Gopalswamy
NASA Goddard Space Flight Center, Greenbelt, MD 20771, USA
e-mail: nat.gopalswamy@nasa.gov

N. Gopalswamy et al. (eds.), *Heliophysical Processes*, Astrophysics and Space Science Proceedings, DOI 10.1007/978-3-642-11341-3_4,

heliospheric termination shock. When CMEs arrive at Earth, they can couple to the magnetosphere causing intense geomagnetic storms, which have implications to all layers of Earth's atmosphere and the ground. This chapter provides an overview of CMEs and flares, the two main aspects of large-scale solar eruptions. Several review articles exist on these topics (see the articles in the recent Geophysical Monographs Gopalswamy et al. 2006a; Song et al. 2001). A more detailed description of the eruption events can be found in (Gopalswamy 2007).

2 A Large-Scale Eruption Illustrated

CMEs have different manifestations depending on the wavelength of observation and the heliocentric distance. CMEs originate from regions on the Sun where the magnetic field lines connect opposite polarities. These regions are the active regions and filament regions, where the magnetic field strength is elevated with respect to the quiet Sun. Most active regions contain sunspots and also filaments. Quiescent filament regions have no sunspots. Figure 1 has a magnetogram and an H-alpha image showing active regions as compact magnetic regions and filament regions as diffuse magnetic regions. Both types of magnetic regions are potential sources of CMEs. Filaments consist of cool material (∼8,000 K) compared to the hot (∼2 MK) corona. Filaments are suspended in the corona and are roughly aligned with the polarity inversion line of the magnetic regions, while their ends are rooted in opposite

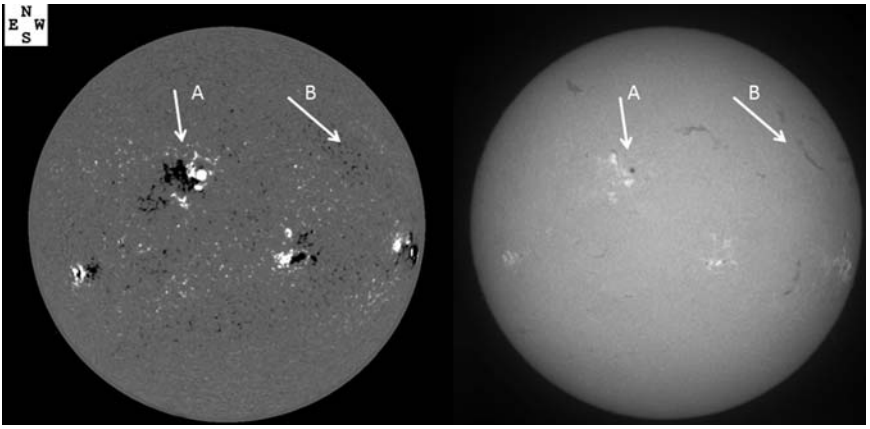

Fig. 1 A line of sight magnetogram from the Big Bear Solar Observatory taken at 15:21:03 UT (*left*) and an H-alpha image from the Kanzelhoehe observatory taken at 08:14:58 (*right*) both on 2005 May 13. In the magnetogram, white and black represent positive (north) and negative (south) magnetic polarities, respectively. The elongated dark features in the H-alpha image are the filaments. One of the active regions (AR 10759) is marked "A". One of the filaments is marked "B". Note that the active region magnetic fields are intense and the filaments are generally thin. In the filament regions, the magnetic field is also enhanced compared to the quiet Sun, bipolar, and more diffuse

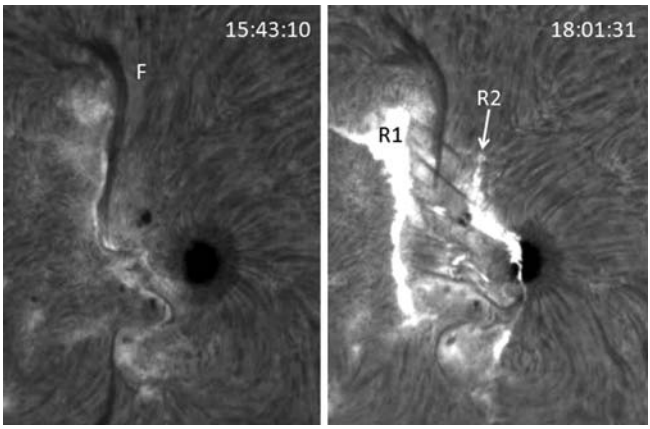

Fig. 2 Two H-alpha images of active region AR 10759 observed on 2005 May 13 at the Big Bear Solar Observatory (BBSO). Each image is of 331 × 351 pixels (pixel size = 0.6 arc sec). (*left*) before eruption and (*right*) after eruption. The elongated dark feature is the filament. Two sunspots of positive polarity can be seen to the west of the filament. In the right side image, part of the filament has disappeared due to eruption and two ribbons (R1, R2) on either side of the filament have appeared. The dark features connecting R1 and R2 are the post-flare loops at a temperature of ∼10,000 K. Courtesy: V. Yurchyshyn

polarity patches. In coronal images, hot loop structures can be seen overlying the filaments. During an eruption, the filament is ejected from the Sun (wholly or partially) including the surrounding coronal material. Thus a CME typically contains multithermal plasma. During the eruption process, the filament gets heated and hence may not remain cold for long in the interplanetary medium.

Figure 2 shows an eruption imaged in H-alpha wavelengths from the region A in Fig. 1. In the pre-eruption image, one can see the vertical dark filament (F) with two sunspots on the western side. After the eruption, one can see two vertical bright ribbons (R1, R2), characteristic of eruptive flares. The ribbons indicate energy input to the chromosphere, thought to be due to electrons from the energy release site just beneath the erupting filament in the corona. The ribbons represent the eruptive flare and the total area of the ribbons is used as a measure of the flare size. The ribbons mark the feet of an arcade of loops thought to be formed due to reconnection. Some of these loops can be seen as dark features connecting R1 and R2. These "post-eruption" loops are roughly perpendicular to neutral line, while the flare ribbons are roughly parallel to the neutral line. The whole arcade can be seen in coronal images obtained in extreme-ultraviolet, X-ray, and microwave wavelengths. Figure 3a shows the photospheric magnetogram and the coronal (potential) magnetic field lines extrapolated from the photospheric field in the active region that produced the eruption. In Fig. 3c one can see the entire arcade in a coronal image at 171 Å obtained by the TRACE satellite. Note the close resemblance between the potential field lines and the post-eruption arcade, in contrast to the pre-eruption coronal structures (Fig. 3b), which are almost aligned along the neutral line. Such

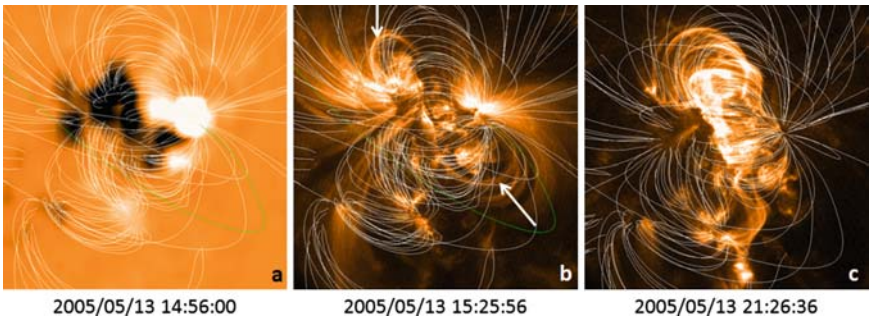

Fig. 3 Magnetic structure in AR 10759 revealed by (**a**) low-resolution photospheric magnetogram at 14:56:00 UT before the eruption (*white* is positive and *dark* is negative) with computed potential field lines (*thin white lines* are closed and the *green line* is open); (**b**) TRACE 171 Å image at 15:25:56 UT showing non-potential coronal structures (two highly sheared coronal loops are pointed by *arrows* with foot-points on either side of the neutral line; (**c**) TRACE 171 Å image of the post-eruption arcade at 21:26:36 UT. Computed potential field lines are also shown superposed. Courtesy: K. Schrijver and M. DeRosa

non-potential structures represent storage of magnetic energy in the corona, which is released during the eruption in the form of thermal energy (flare heating) and kinetic energy (CME). Figure 4 shows a large-scale disturbance in the corona surrounding the active region revealed by EUV images obtained by the Solar and Heliospheric Observatory (SOHO). Such disturbances are coronal waves (MHD fast mode waves or shocks depending on the speed) surrounding the erupting CME. The EUV disturbance has a size of $\sim 0.4\,R_\odot$ at 16:37 UT. The disturbance spreads over the entire solar disk by 17:07 UT as can be seen in Fig. 5. Detection of such large-scale EUV disturbances has become a standard way of identifying the solar source of CMEs. The white light CME in Fig. 5 taken about 15 min after the EUV image clearly shows the close connection between the EUV disturbance and the CME in white light. The soft X-ray flare in Fig. 5 also shows the close connection between flares and CMEs. The current paradigm for CMEs is that the flare reconnection process creates a flux rope (or builds upon a pre-existing one), whose outward motion causes the disturbance seen in white light as the CME.

The CME first appeared at a heliocentric distance of $\sim 4.6\,R_\odot$ just above the occulting disk (which has a radius of $3.7\,R_\odot$) at 17:12 UT (see Fig. 6). The disturbance can be seen simultaneously at the north and south edges of the occulting disk, suggesting that it was elongated in the north-south direction as is clear from the white light image taken at 17:42 UT (Fig. 6). Between 17:12 and 17:42 UT, the leading edge of the white light feature moved a distance of $\sim 4.4\,R_\odot$, indicating a speed of $\sim 8.8\,R_\odot/\mathrm{h}$ or $\sim 1{,}700\,\mathrm{km\,s^{-1}}$. Since the eruption occurred on the frontside of the Sun that faces Earth, the CME should reach Earth (which is $\sim 214\,R_\odot$ away from the Sun) in a day or so. In fact, the leading part of the CME-driven shock arrived at Earth (see Fig. 7a) on 2005 May 15 at 02:19 UT, which is a little more than a day because CMEs undergo deceleration due to interaction with the solar wind. The speed of the CME heading towards Earth cannot be measured accurately because of the occulting

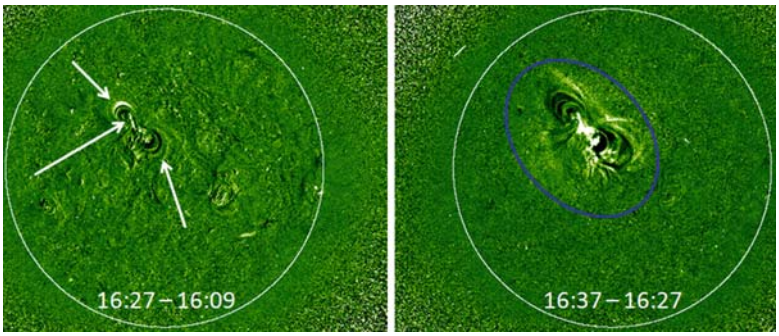

Fig. 4 EUV images at 195 Å obtained by the Solar and Heliospheric Observatory (SOHO) showing changes in the sheared loops (*left* at 16:27 UT) and large-scale diffuse disturbance surrounding the active region (*right* at 16:37 UT). These are running difference images (previous image subtracted from the current image to reveal changes taking place during the interval between the two images). In the left image, the three *arrows* point to significant changes: the central brightening near the neutral line (corresponding to the beginning of the H-alpha ribbons) and the expansion of the sheared loops noted in Fig. 3b. In the right image, the post-eruption arcade near the neutral line has expanded; the large-scale disturbance is shown encircled

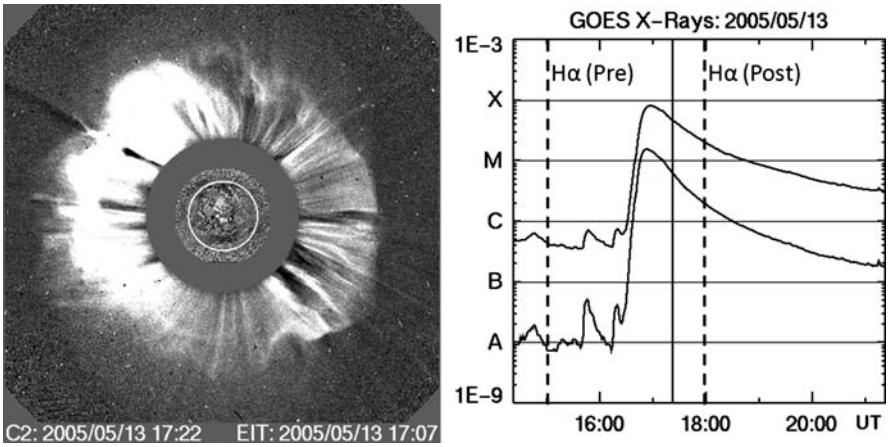

Fig. 5 (*left*) White light CME detected by SOHO in its C2 telescope of the Large Angle and Spectrometric Coronagraph (LASCO) on 2005 May 13 at 17:22 UT. Superposed on this image is a EUV difference image from SOHO/EIT at 17:07 UT. Note that the EUV disturbance has spread over the entire solar disk compared to the image at 16:37 shown in Fig. 4. (*right*) Soft X-ray light curve in two energy channels (1–8 Å upper curve; 0.4–5 Å lower curve). The soft X-ray detector has no spatial resolution, but most of the flare emission comes only from AR 10759. The time of the LASCO image is marked by the solid vertical line. The two dashed lines correspond to the pre and post-eruption H-alpha pictures shown in Fig. 2

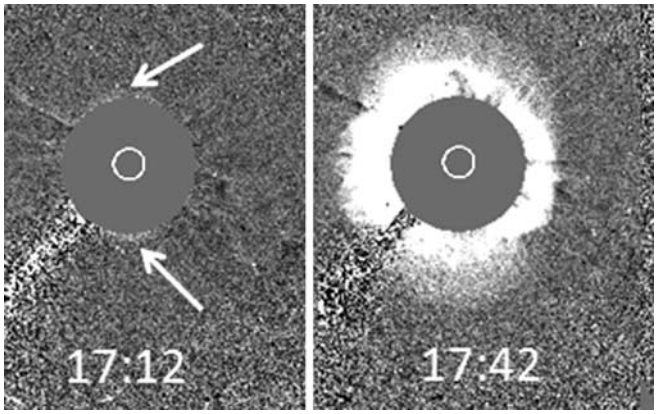

Fig. 6 White light CME detected by SOHO in its C3 telescope of LASCO. These are difference images with previous frame subtracted. In the left frame the CME appears above the occulting disk (pointed by *arrows*). In the right frame, the CME has expanded significantly. The occulting disk is employed by the coronagraph to block the photospheric light so weak coronal features can be imaged. The white circle at the center of the images represents the optical disk of the Sun

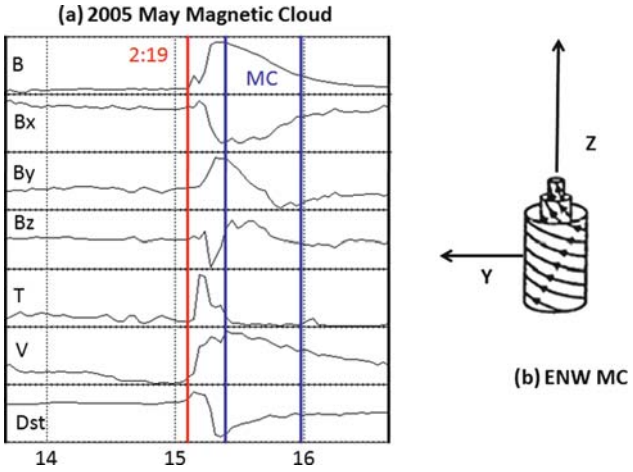

Fig. 7 (**a**) Plots of the magnetic field magnitude (B), its three components (Bx, By, Bz) in Geocentric Solar Magnetospheric (GSM) coordinates, temperature, solar wind speed, and the Dst index (all in arbitrary units). The origin of the X-axis roughly corresponds to the beginning of activities in AR 10759. The vertical line at 02:19 UT on 2005 May 15 is the time of arrival of the shock at the ACE spacecraft at the L1 point. The vertical line at 11:00 UT the same day is the arrival time of the magnetic cloud that was driving the CME. The Dst index shows an intense geomagnetic storm, with an intensity of −263 nT. All the physical quantities change drastically at the arrival of the shock and magnetic cloud. (**b**) Flux-rope structure of the ICME as derived from the By, and Bz components. The Bz component in the MC always points to the north, while the By component rotates smoothly from the east (E) to west (W). Thus the MC is classified as a ENW cloud

disk, which introduces additional uncertainty in the CME speed. Unlike the 2-dimensional images of CMEs near the Sun, the in-situ measurements are only along a single trajectory through the CME as it moves past the observing spacecraft. The measurements shown in Fig. 7a indicate that the disturbance lasted for a period of $\sim$1 day. The interplanetary CME (ICME) had a flux rope structure with its axis in the Z-direction, but it was pointing to the north (see Fig. 7b). The shock sheath ahead of the flux rope had an intense south-pointing field, which merged with Earth's magnetic field and caused a very intense geomagnetic storm (measured by the Dst (Disturbance Storm time) index, which reached -263 nT). A CME such as the one on 2005 May 13, which results in a Dst index ≤ -50 nT is said to be geoeffective.

The shock at 1 AU is directly detected by spacecraft in the solar wind. A shock near the Sun has to be inferred from remote observations such as at radio wavelengths and from energetic particles. When the CME speed near the Sun exceeds the coronal Alfven speed, it can drive a shock. The shock accelerates electrons and ions (solar energetic particles or SEPs for short). The accelerated electrons produce radio emission by interacting with the ambient corona. Accelerated ions and electrons also propagate to the detectors in near-Earth space within tens of minutes. Shocks continue to accelerate SEPs as they propagate into the IP medium, so they are continuously detected until the shock reaches the observing spacecraft, when a sudden increase in SEP intensity is observed. The intensity increase is referred to as an energetic storm particle (ESP) event because a geomagnetic storm usually follows due to the sheath and/or ICME behind the shock. In the 2005 May 13 event, a metric type II burst was observed at 16:38 UT, coincident with the large-scale EUV disturbance. A more intense type II was observed by the Wind/WAVES experiment in the IP medium starting around 17:00 UT.

Figure 8 shows the SEP event as detected by the Geostationary Operational Environment Satellite (GOES) and the radio dynamic spectrum (frequency vs. time plot of the radio intensity) obtained by the Wind/WAVES experiment. Both the SEPs and the type II burst are thought to be due to the CME-driven shock. From Fig. 8, we see that SEPs are observed more than an hour after the CME onset near the surface. However, when we account for the propagation time of 10 MeV protons, the SEP release time is $\sim$17:18 UT, when the CME was at a heliocentric distance of $\sim 7\,R_\odot$. Note that SEPs are observed when the shock is near the Sun until its arrival at the spacecraft at 02:19 UT on May 15, marked by the ESP event. During the ESP event, the proton intensity in the 10 MeV channel jumps from 100 to 3,000 pfu. The SEP intensity drops significantly in the sheath and Magnetic Cloud (MC) regions.

The type II burst occurs at the local plasma frequency (fp) or it harmonic (2fp). Assuming the radio emission to be at the harmonic, one can estimate the plasma density (n) at the heliocentric distance of the CME since $fp = 9 \times 10^{-3} n^{1/2}$, where fp is in MHz and n is in cm^{-3}. For example, the type II burst at 17:42 UT occurs at 0.6 MHz, so fp = 0.3 MHz and $n \sim 1.1 \times 10^3\,cm^{-3}$. At this time, the CME is at a height of $\sim 9.0\,R_\odot$. The actual height of the CME can be estimated to be $\sim 11\,R_\odot$ assuming that the CME is cone-shaped. As the CME propagates away from the Sun, the shock ahead of it passes through layers of decreasing plasma density and hence producing radio emission at decreasing frequency. Thus the type II burst can be

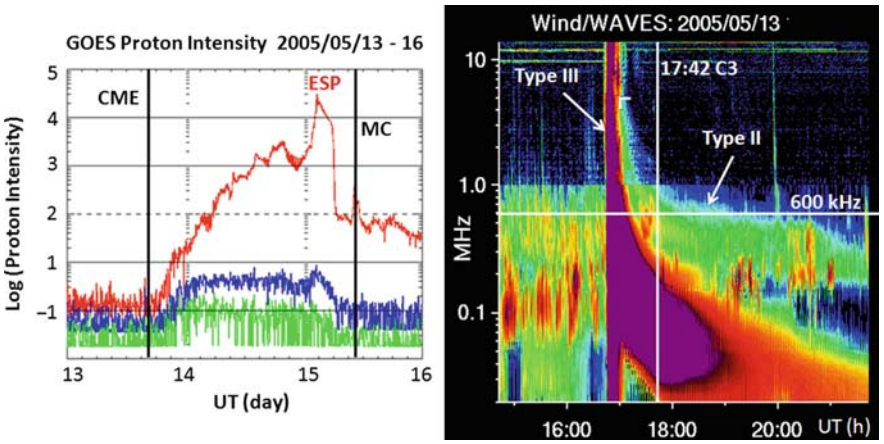

Fig. 8 (*left*) Intensity plots of SEPs (protons) during the 2005 May 13 CME in three energy channels >10 MeV (*red*), >50 MeV (*blue*), and >100 MeV (*green*) as detected by the GOES satellite. The SEP intensity is in particle flux units (pfu); 1 pfu = 1 proton $(\mathrm{cm}^2\,\mathrm{s}\,\mathrm{sr})^{-1}$. The sharp spike in the SEP intensity (>10 MeV channel) is the ESP event. Approximate onset time of the CME at the Sun (16:37 UT on May 13) and near Earth (MC arrival at 11 UT on May 15) are marked by the vertical black lines. (*right*) Dynamic spectrum obtained by the Radio and Plasma Wave (WAVES) experiment on board the Wind spacecraft. The type III burst is indicative of electron beams from the eruption site. The type II burst is due to nonthermal electrons accelerated at the CME-driven shock. The type II radio emission occurs at ∼600 KHz when the CME was last seen in the coronagraph image at 17:42 UT (indicated by the vertical line)

used to track the CME-driven shock beyond the coronagraphic field of view. For the 2005 May 13 CME, the type II radio emission was observed all the way to the Wind spacecraft (where the local plasma frequency was ∼30 kHz).

The 2005 May 13 event discussed above is a well-observed CME with all the associated phenomena such as a flare (H-alpha and soft X-ray), filament eruption, EUV wave, white-light CME, type II radio burst (metric and IP), SEP, ICME with shock, and geomagnetic storm. The white-light CME is also a halo CME in that the CME appears to surround the occulting disk in sky-plane projection (Howard et al. 1982). CMEs like this make significant impact on the heliosphere and hence are important in deciding space weather. Space weather refers to the conditions in the space environment that is hazardous to space or ground based technological systems or to human health or life. SEPs, geomagnetic storms, and ionospheric storms are some of the space weather effects directly linked to CMEs.

3 CME Properties

CMEs have been studied extensively using data from several spaceborne coronagraphs since the early 1970s and the ground-based Mauna Loa K-coronameter (see Gopalswamy 2004; Kahler 2006 for recent reviews.) The statistical properties of

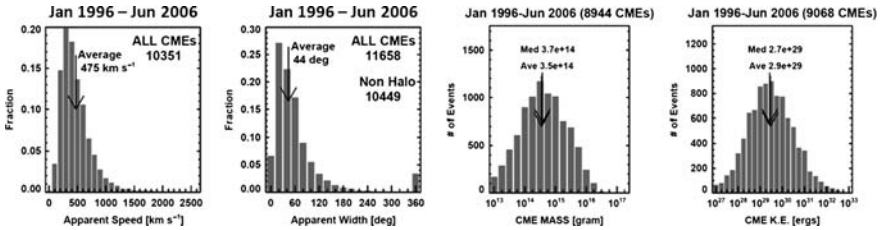

Fig. 9 Speed, width, mass and kinetic energy distributions of CMEs observed over most of solar cycle 23 (1996–2006)

CMEs based on SOHO observations can be summarized as follows: (1) the CME speed varies over two orders of magnitude from ∼20 to more than 3,000 km s^{-1}, with an average value of 475 km s^{-1}. (2) The CME angular width ranges from <5° to 360° (halo CMEs). The average width of CMEs with width <120° is ∼44°. Almost 90% of the CMEs have width <120°, and only ∼3.5% have an apparent width of 360°. About 11% of CMEs have width ≥120°. The speed and width distributions of CMEs are shown in Fig. 9. (3) CMEs with above-average speeds decelerate due to coronal drag, while the lower speed ones accelerate. CMEs with speeds close to the average speed do not have observable acceleration. (4) CME mass ranges from a few times 10^{12} g to more than 10^{16} g with an average value of 3.4×10^{14} g (Gopalswamy 2004). The corresponding kinetic energies range from $\sim 10^{27}$ erg to more than 10^{33} erg, with an average value of 2.9×10^{29} erg (see Fig. 9). (5) Within the field of view of the Large Angle and Spectrometric Coronagraph (LASCO), CMEs occur with an average rate of <0.5 per day (solar minimum) to >6 per day (solar maximum). High-latitude (>60°) CMEs contribute to the CME rate significantly during solar maximum. (6) The average speed of CMEs (averaged over Carrington Rotation periods) increases by a factor of 2 from ∼250 km s^{-1} during solar minimum to ∼550 km s^{-1} during solar maximum. (7) CMEs contain coronal material at a temperature of ∼ a few MK in the outer structure with cool prominence material (∼8,000 K) in the core. (8) About a third of the ICMEs observed at 1 AU have flux rope structure (magnetic clouds). Non-cloud ICMEs generally originate at larger distances from the Sun center. (9) All CMEs are associated with flares, but there are many flares not associated with CMEs. (10) Type II radio bursts are signatures of electron acceleration by CME-driven shocks (Gopalswamy 2006). (11) Large SEP events are always associated with energetic CMEs.

4 CMEs and Flares

Mass motion in the form of H-alpha ejecta during flares has been identified as one of the key aspects of flare – CME association because ∼90% of such flares are associated with CMEs (see, e.g., Kahler 1992; Munro et al. 1979). On the other

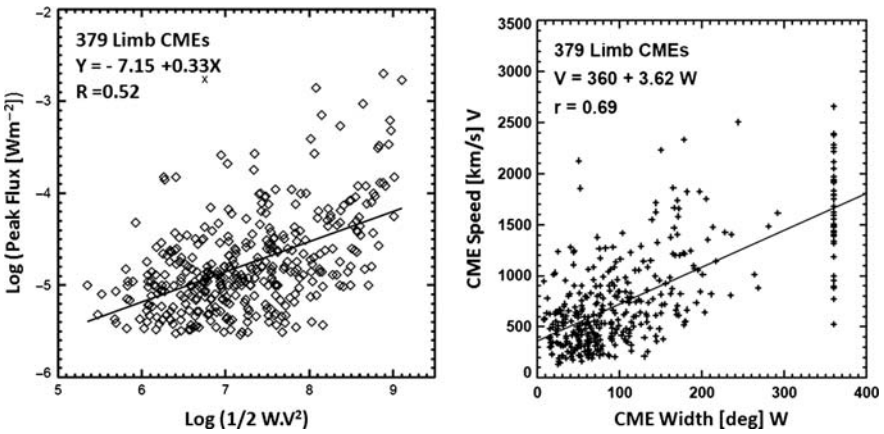

Fig. 10 Scatter plot between (*left*) peak soft X-ray flux and proxy kinetic energy and (*right*) CMEs width and speed. The data are for limb eruptions central meridian distance ($\geq 60^{\circ}$)

hand not all flares are associated with CMEs. In fact, even some X-class flares are not associated with CMEs. Like CMEs, flares also occur from closed field regions, so, the released energy must go entirely into heating in flares without CMEs. There is some evidence that flares without CMEs are generally much hotter: the average temperature of flares without CMEs was found to be 18.4 MK compared to 11.7 MK for flares with CMEs (Kay et al. 2003).

For flares with CMEs, there is a reasonable correlation between flare size in soft X-rays and the CME kinetic energy (Hundhausen 1999; Moon et al. 2002). The correlation coefficient is only 0.53, suggesting that the partition between heating and mass motion may not be uniform in all eruptions. Figure 10a shows a similar plot between peak soft X-ray flux and the quantity $0.5\,WV^2$, where W is the CME width and V is the CME speed for a set of 342 CMEs associated with flare originating close to the limb. The limb events were chosen to avoid projection effects in the measured speeds. We take $^1/_2WV^2$ to be the kinetic energy of CMEs because the CME mass has been shown to be proportional to the CME angular width (Gopalswamy et al. 2005a). The correlation coefficient is also very similar to previous values. Figure 10b shows a reasonable correlation between CME width and speed. However, all flares are not associated with CMEs. In flares without CMEs, all the released energy must go into heating. On the other hand, in flares with CMEs, the free energy is partitioned between heating (soft X-ray flares) and mass motion (CMEs). A recent study of flares with and without CMEs involving parameters such as peak flux, fluence, and duration of soft X-ray flares found that they all followed a power law (Yashiro et al. 2006). However, the power law index for the CME-associated flares was >2, while that for CMEless flares was <2. This suggests that in flares without CMEs, the free energy goes entirely into heating the corona (Hudson 1991).

Studies on temporal correspondence between CMEs and flares have concluded that CME onset typically precedes the associated X-ray flare onset by several

minutes. On the other hand, tiny flare-like brightenings and filament activation is known before the lift off of a filament (Gopalswamy et al. 2006b). In the 2005 May 13 example discussed above, the soft X-ray flare was reported to start at 16:13 UT. H-alpha movie shows filament activation more than 10 min before. The filament activation may indicate some kind of instability in the system. On the other hand the small-scale brightenings may push the system towards eruption. Thus, the flare-CME relationship is generally complex.

The spatial relation between flares and CMEs has also been studied by many authors (Harrison 2006; Kahler et al. 1989; Yashiro et al. 2008). The general consensus in the pre-SOHO era was that the flare was located anywhere under the span of the CME. However, using the extensive SOHO data base on CMEs, it was recently found that the CME leading edge is typically located radially above the flare location (Yashiro et al. 2008). They studied a set of 496 flare-CME pairs with solar sources away from the disk center (central meridian distance (CMD) $> 45°$). They found that the offset between the flare position and the central position angle (CPA) of the CME has a Gaussian distribution centered on zero (see Fig. 11). This finding calls for a closer flare-CME relationship as implied by the CSHKP eruption model (Yashiro et al. 2008). In fact, it has become common practice to identify the solar source of CMEs as the flare location derived from H-alpha or soft X-ray imaging observations.

Another important near-surface activity often associated with CMEs is prominence eruption (Gopalswamy et al. 2003; Munro et al. 1979; St. Cyr and Webb 1991). Sometimes CMEs are classified as flare-related and prominence-eruption related. This classification, however, is not very sharp because flares are also associated with prominence eruptions as demonstrated in Sect. 2. In fact, flares and filament eruptions correspond to the heating and mass motion aspects of eruptions, both of which are present in all CMEs. This classification may be meaningful for CMEs from

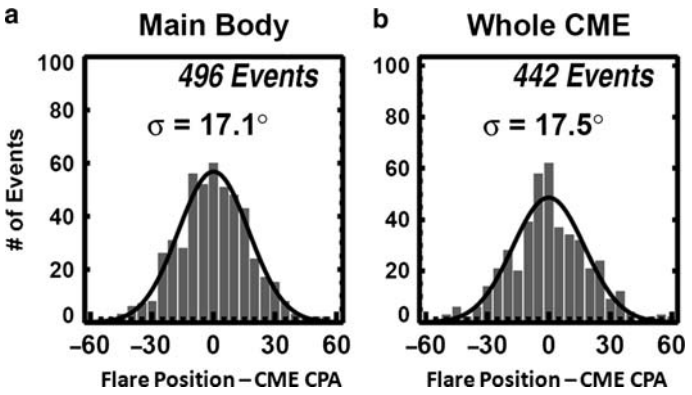

Fig. 11 Distributions of the offset of flare positions with respect to the central position angle (CPA) of the associated CMEs. The standard deviation (σ) obtained by fitting a Gaussian to the distribution (*solid curve*) is shown on the plot. The main body (probably the flux rope) and the whole CME (including the diffuse outer part) show similar relationship

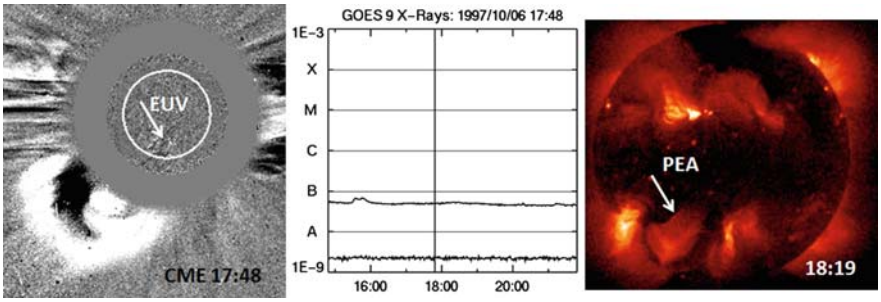

Fig. 12 (*left*) The CME on 1997 October 6 in the LASCO/C2 field of view with the EUV disturbance pointed by *arrow*. (*middle*) GOES soft X-ray plot showing no significant enhancement above the B-level background at the time of the CME marked by the vertical line. (*right*) Yohkoh Soft X-ray Telescope (SXT) image showing the post-eruption arcade (PEA) in the quiet Sun region

quiescent filament regions, but even there, one can see large-scale post-eruption arcades in soft X-ray and EUV images, but they are not intense enough to be above the background in GOES soft X-ray plots. Figure 12 shows an example. The large CME on 1997 October 6 originated from a quiescent filament region (the eruption can be seen as a EUV disturbance in the EIT image superposed on the LASCO image). The GOES X-ray background was very low, but the eruption does not show up in GOES soft X-rays. However, a large-scale post-eruption arcade (PEA) can be seen in the soft X-ray image taken at 18:19 UT. The arcade lasted for several hours.

5 CMEs, Shocks, Type II Bursts, and SEPs

Shocks have been inferred from metric type II radio bursts, which have been studied for more than six decades (see Gopalswamy 2006 for a review). There was a lot of controversy regarding the origin of shock waves (Cliver et al. 1999) responsible for the metric type II bursts (flare blast waves or CME-driven shocks). The root cause of the controversy was the observation that a third of metric type II bursts was not associated with CMEs. However, it was found that most of the solar eruptions associated with CMEless type II bursts originated close to the disk center. Coronagraphic observations favor CMEs originating from close to the limb. Only very energetic eruptions from close to the disk center will appear as halo or partial halo CMEs above the occulting disk (Cane et al. 2007). For example, when solar sources close to the limb are considered, all the metric type II bursts are associated with CMEs (Gopalswamy et al. 2005a; Munro et al. 1979). Therefore, all the metric type II bursts may be due to CME-driven shocks. Type II bursts at decameter-hectometric (DH) wavelengths originating from the near-Sun interplanetary medium (beyond about 3 $R_\odot$) are all associated with fast and wide CMEs even if the eruption occurs near the disk center. Some type II bursts occur at various bands from metric (near Sun) to kilometric (near Earth) wavelengths. CMEs associated with these mkm type II bursts have the highest speed and width. There is a progressive increase in speed and fraction of halo CMEs as one goes from CMEs associated with metric, DH,

and mkm type II bursts. The number of type II bursts also decreases in the same order suggesting that only the most energetic of CMEs can produce type II bursts throughout the inner heliosphere. Another interesting result is that the speed and fraction of halos of CMEs associated with large SEP events is nearly identical to those of CMEs associated with mkm type II bursts. The reason is that the same intense shock accelerates electrons (observed as type II bursts) and ions (observed as SEP events in the interplanetary medium) (Gopalswamy et al. 2008).

White-light observations of shocks are rare, mainly because the shocks are very thin and the standoff distance between the flux rope and the shock is very small close to the Sun. Faint disturbances at the flanks of halo CMEs have been identified as shocks (Sheeley et al. 2000). A few other CMEs with possible shocks ahead of them have also been reported (Vourlidas et al. 2003). Figure 13 shows another example in which the leading diffuse feature can be identified as a shock. This event has a distinct flux rope and CME core, so the outer edge of the diffuse feature can be identified as a shock. In direct images, the diffuse feature was not visible, but a kink (marked S in Fig. 13) in the streamer indicates a disturbance. In the difference image, the kink location is seen as the intersection of the diffuse feature with the streamer. The diffuse feature itself can be identified as the shock sheath.

The close physical relationship among large flares (M and X class), fast and wide coronal mass ejections, DH type II radio bursts (including mkm type II bursts), CME-driven shocks observed *in situ*, and large SEP events is revealed in Fig. 14. We have plotted the number of events under each category summed over Carrington rotation periods. The numbers are close to one another having a similar variation with the solar cycle. The rates peak in the solar maximum phase (1999–2002), but there are occasional large spikes, which are due to some active regions that are prolific producers of eruptions in quick succession. There are many major flares, which are not associated with CMEs or type II bursts and hence the higher rate for M- and X-class flares. All the other events are physically related: FW CMEs

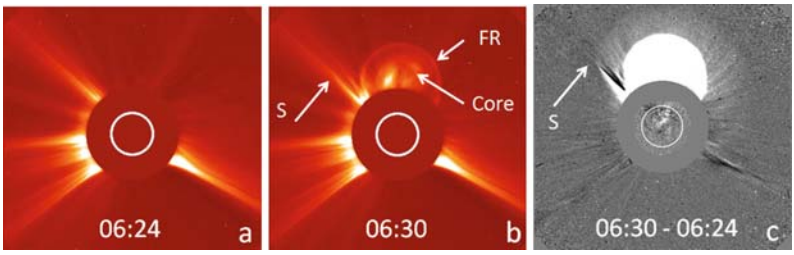

Fig. 13 Possible shock observed in a SOHO/LASCO/C2 image on 2005 January 15. (**a**) pre-event LASCO image at 06:24 UT. (**b**) LASCO image at 06:30 UT with CME appearing above the northwest limb with a flux rope (FR) structure and a bright core; a kink is obvious in the streamer at the location marked by "S". (**c**) Difference image (06:30 minus 06:24), which shows the coronal change over a period of 6 min; this image shows the diffuse structure (S), which is likely to be the shock. The diffuse structure envelopes the flux rope and is more extended than the flux rope. A EUV difference image is superposed on the LASCO difference image to show that the solar source is located in the northern hemisphere of the Sun

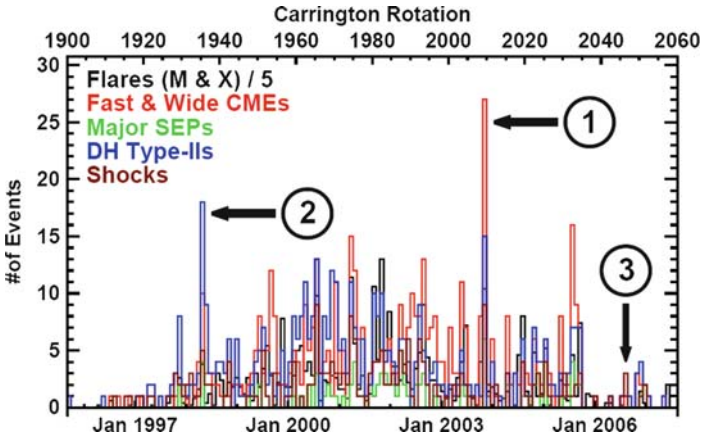

Fig. 14 Numbers of major flares (divided by a factor of 5 to fit the scale), fast and wide (FW) CMEs, DH type II bursts (including mkm type II bursts), large SEP events, and in-situ shocks plotted as a function of time. Large SEP events are those with proton intensity in the >10 MeV energy channel exceeding 10 pfu; pfu is the particle flux unit defined as the number of particles/(cm^2 s sr). The numbers are binned over Carrington Rotation periods (∼27 days). Examples of FW CMEs without type II bursts and SEPs (1), DH type II without FW CMEs (2), and interplanetary shocks without DH type II bursts and SEPs (3) are indicated by *arrows*

drive shocks, which accelerate electrons (producing type II radio bursts) and ions (observed in situ as SEP events). The shocks are also detected in situ when they survive the Sun-Earth transit, which can last anywhere from <1 day to >3 days. Figure 14 reveals some exceptions: (1) FW CMEs without type II bursts, (2) DH type II bursts without FW CMEs, and (3) in-situ shocks not accompanied by other types of energetic events. FW CMEs without type II bursts indicate that occasionally the Alfven speed in the ambient medium can be very high (up to 1,600 km s^{-1}). DH type II bursts (and sometimes SEP events) associated with CMEs as slow as ∼400 km s^{-1} indicate that very low coronal Alfven speed (<400 km s^{-1}) can prevail in the corona. Shocks without associated type II burst or SEP event generally form at large distances from the Sun and are extremely weak. These are likely to be "subcritical" shocks, which do not accelerate particles in significant numbers (Mann et al. 2003).

It is clear that every large SEP event is associated with a unique CME that is highly energetic. In the above discussion, we have tacitly assumed that the SEPs are accelerated by the CME-driven shock supported by the direct evidence provided by the ESP events. The flare reconnection site is another place where particles are accelerated. Hard X-ray bursts and type III radio bursts during flares without CMEs provide strong evidence for particle acceleration by a non-shock process. Historically, SEPs produced in flares and propagating into the IP medium are referred to as "impulsive events", which are of very short duration and small intensity compared to the large SEP events (also known as the gradual events). Similarly the gradual SEP events were also studied only from the point of view of the associated CMEs (and

shocks). Since each of the CMEs associated large SEP events are also associated with a major flare, one naturally expects contributions from the flares. Flare particles in CME events are also expected to be of higher intensity because of the larger flare size compared to those associated with impulsive events. While there is no question that the two mechanisms operate in nature, but what was missed is the fact that they operate simultaneously in every CME event. There may even be interaction between the two sources in that the flare particles may pass through the shock region and get further accelerated. There is an ongoing debate on the relative contribution from the flare and shock sources (Cane et al. 2007; Tylka and Lee 2006).

6 CMEs and Geomagnetic Storms

Geomagnetic storms occur when an interplanetary structure such as an ICME containing southward magnetic field arrive at Earth's magnetosphere and reconnects with the geomagnetic field. The storm strength is measured by one of the indices such as the Dst index. A white-light CME observed near the Sun may result in a shock, sheath, and the driving ICME at 1 AU. The shock and the ICME front boundary delineate the sheath region. A CME can be geoeffective due to a south-pointing magnetic field component in the sheath region or in the ICME (ejecta) region. When the ICME is an MC, then one can infer which section of the MC is geoeffective based on the magnetic structure of the MC (flux rope orientation with respect to the ecliptic plane and its sense of rotation). Although most of the large geomagnetic storms are caused by magnetic clouds, non-cloud ejecta can also be geoeffective. Depending on the magnetic structure in the sheath and cloud portions, the following situations are encountered: (1) sheath and MC are geoeffective, (2) sheath alone is geoeffective, (3) MCs alone are geoeffective, and (4) none are geoeffective. The last situation arises when neither the sheath nor the MC contains south-pointing magnetic field component. When both sheath and MC are geoeffective, the Dst profile can be complex depending on the location of the south-pointing field in the sheath and cloud portions.

6.1 Halo CMEs

Halo CMEs constitute a special population selected by the nature of coronagraphic observations: slow and narrow CMEs originating from close to the Sun center are not usually seen in coronagraph images. Typically, fast (CME speed $\geq$900 km s^{-1}) and wide CMEs (width $\geq$60°) appear as halos. Occasionally some halos are slow. Figure 15 shows that the average speed of disk halos (with the central meridian distance (CMD) of the solar source $\leq$45°) is $\sim$933 km s^{-1}, which is close to that of the backside halos (977 km s^{-1}). However, the average speed of limb halos (45°<CMD$\leq$90°) is $\sim$1,548 km s^{-1}. There are two reasons for the higher speed

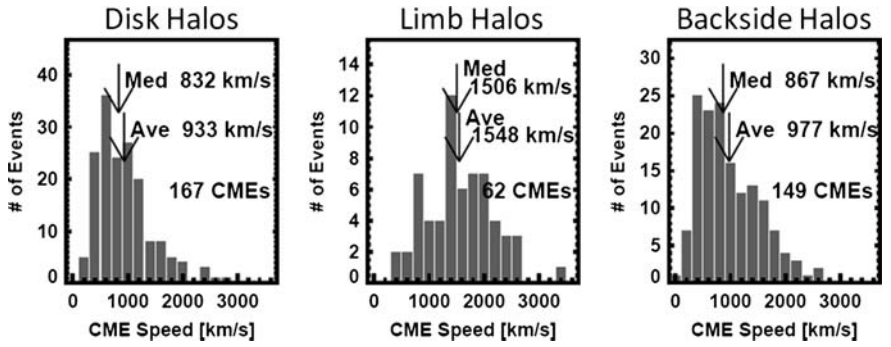

Fig. 15 Speed distributions for (*left*) disk halos (CMD $\leq 45°$), (*middle*) limb halos ($45° <$ CMD $\leq 90°$), and (*right*) backside halos (CMD $> 90°$)

of limb halos: (1) the disk halos originate close to the disk center, so their speeds are severely affected by projection effects in contrast to the limb halos, which are not significantly affected by projection effects; (2) halo CMEs by definition have to surround the occulting disk, so a CME originating close to the limb should travel very fast to be observed above the opposite limb. Thus only the fastest limb CMEs can become halos. The backside halos are far behind the limb and hence are subject to projection effects similar to the disk halos. The average speed of all halos is $\sim$1,000 km s^{-1}, which is more than two times the average speed of all CMEs. For such speeds, the average width of the CMEs can be inferred as $\sim$180° from Fig. 10b. Thus the halo CMEs are generally more energetic. This is further confirmed by the fact that the average size of soft X-ray flares associated with halo CMEs is an order of magnitude larger than the average size of all the flares observed in solar cycle 23 (Gopalswamy et al. 2007). As Fig. 10 shows, higher flare intensity implies higher kinetic energy for the associated CMEs. Higher kinetic energy enables the CMEs to propagate far into the interplanetary medium. From coronagraphic observations alone, it is difficult to say whether a halo CME is frontsided or not. In Fig. 5 the halo CME is front sided (i.e., Earth-directed) as can be seen in the superposed EUV images. We need to combine coronagraphic observations with coronal images obtained in EUV, soft X-ray, microwave, or H-alpha wavelengths to identify disk activity.

6.2 Geoeffective CMEs

The source locations of halo CMEs are compared with those of ICMEs in Fig. 16. We have plotted the solar sources MCs and non-cloud ICMEs separately. MCs have higher magnetic field, smooth rotation, and low proton temperature (indicating flux rope structure Burlaga et al. 1982). Non-cloud ICMEs do not appear as flux ropes in in-situ observations. The events in Fig. 16 are the most energetic events in the

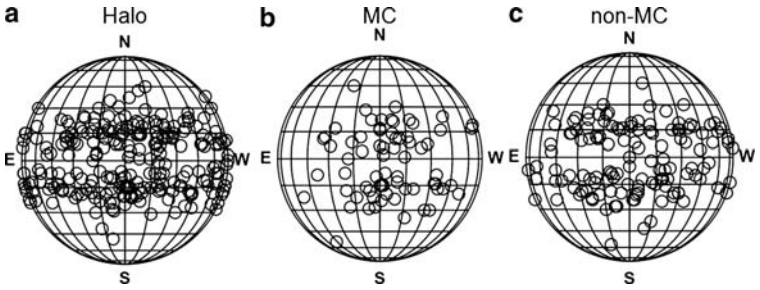

Fig. 16 Solar sources of halo CMEs (**a**) and shock-driving ICMEs (**b**)

heliosphere and they are due to energetic CMEs from the Sun. The close similarity between halo CME sources and the sources of ICMEs indicate that there is high degree of overlap between halo CMEs and the CMEs that become ICMEs. Those ICMEs that have south-pointing magnetic field in the ejecta part or sheath part produce geomagnetic storms. The product of the speed and magnetic field strength in ICMEs has been shown to have a good correlation with the intensity of geomagnetic storms. In a step further, it was recently shown that CME speed and its product with the magnetic field in the associated ICME have also equally good correlation with the Dst index (Gopalswamy 2008). This raises the possibility of storm prediction based on remote-sensing measurements of CMEs if one can estimate the magnetic field strength and orientation in CMEs when they are still near the Sun.

7 Summary

We have made a significant progress in understanding the origin, propagation and heliospheric consequences of solar eruptions, thanks to the continuous data acquired by the SOHO mission on CMEs and their solar sources. We are also able to understand the kinematic and magnetic connection between the ICMEs observed in the IP medium and the white-light CMEs remote sensed by coronagraphs. Concentrated efforts by NASA's Living with a Star (LWS) program and the US National Space Weather program have promoted efforts to find the chain of connectivity from the Sun all the way to the geospace and ground.

The whole solar cycle worth of CME data from SOHO have taught us that only a small subset of energetic CMEs are responsible for severe heliospheric consequences. This can be easily understood from Fig. 17, which shows the cumulative number of CMEs above a certain speed V. We have marked the average values of various subsets: (1) CMEs associated with metric type II radio bursts (m). (2) CMEs associated with magnetic clouds (MC). (3) CMEs that cause major geomagnetic storms (GEO). (4) Halo CMEs that appear to surround the occulting disk of the coronagraph (HALO). (5) CMEs associated with type II bursts having emission components at all wavelengths (mkm). (6) CMEs producing large solar

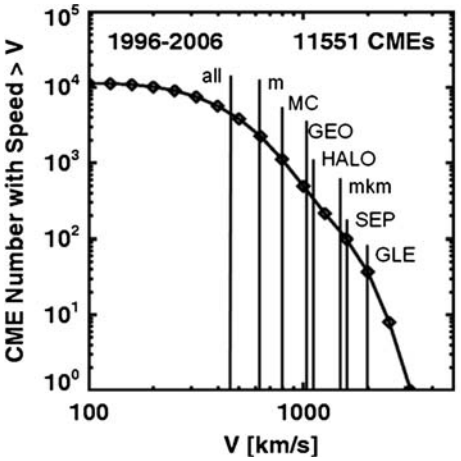

CME population	<V> km/s
All CMEs	471
metric II CMEs	610
MC CMEs	774
Geoeffective CMEs	1042
Halo CMEs	1052
mkm II CMEs	1500
SEP CMEs	1600
GLE CMEs	2000

Fig. 17 Cumulative distribution of CME speeds with the average speeds (<V>) of various special populations marked (*left*) and listed (*right*)

energetic particle (SEP) events. (7) CMEs associated with the ground level enhancement (GLE) in SEPs, which are a subset of SEP events, but associated with the fastest population of CMEs. These are rare events with the average CME speed of $\sim$2,000 km s^{-1} (Gopalswamy et al. 2005b). The three fastest populations (mkm, SEP, GLE) all drive shocks and accelerate particles. The three populations with intermediate speed (MC, GEO, and HALO) represent CMEs that directly impact Earth's magnetosphere. The m population also drives shocks, but very close to the Sun. CMEs faster than 1,000 km s^{-1} contain GEO, HALO, SEP-related, mkm type II related, and GLE-related CMEs. There are $\sim$1,000 CMEs over the solar cycle, which have speeds exceeding $\sim$1,000 km s^{-1}. In other words, $\sim$10% of the fastest CMEs make significant impact on the heliosphere.

References

Burlaga, L.F., Klein, L., Sheeley, N.R. Jr., Michels, D.J., Howard, R.A., Koomen, M.J., Schwenn, R., Rosenbauer, H.: Geophys. Res. Lett. **9**, 1317 (1982)

Cane, H., Richardson, I., VonRosenvinge, T.: Space Sci. Rev. **130**, 301 (2007)

Cliver, E.W., Webb, D.F., Howard, R.A.: Solar Phys. **187**, 89 (1999)

Davis, K.: Ionospheric Radio, p. 580. Peter Peregrinus, London (1990)

Gopalswamy, N.: In: Poletto, G., Suess, S. (eds.) The Sun and the Heliosphere as an Integrated System, p. 201. Springer, New York (2004)

Gopalswamy, N.: In: Gopalswamy, N., Mewaldt, R., Torsti, J. (eds.) Solar Eruptions and Energetic Particles. Geophysical Monograph Series vol. 165, p. 207. AGU, Washington DC. (2006)

Gopalswamy, N.: In: Hasan, S.S., Banerjee, D. (eds.) Kodai School on Solar Physics, vol. 919, p. 275. AIP conference Proceedings. AIP, New York (2007)

Gopalswamy, N.: J. Atmos. Sol. Terr. Phys. **70**, 2078 (2008)

Gopalswamy, N., Shimojo, M., Lu, W., Yashiro, S., Shibasaki, K., Howard, R.A.: Astrophys. J. **586**, 562 (2003)
Gopalswamy, N., Aguilar-Rodriguez, E., Yashiro, S., Nunes, S., Kaiser, M.L., Howard, R.A.: J. Geophys. Res. **110**, 12S07 (2005a)
Gopalswamy, N., Xie, H., Usoskin, I.: In: Acharya B.S., Gupta S., Jagadeesan P., Jain A., Karthikeyan S., Morris S., Tonwar S. (eds.) Proceedings of the 29th International Cosmic Ray Conference. vol. 1, p.169. Tata Institute of Fundamental Research, Mumbai (2005b)
Gopalswamy, N., Mewaldt R., Torsti J. (eds.): Geophysical Monograph Series, vol. 165, p. 385. AGU, Washington DC (2006a)
Gopalswamy, N., Mikic, Z., Maia, D., Alexander, D., Cremades, H., Kaufmann, P., Tripathi, D., Wang, Y.-M.: Space Sci. Rev. **123**, 303 (2006b)
Gopalswamy, N., Yashiro, S., Akiyama, S.: J. Geophys. Res. **112**, A06112 (2007)
Gopalswamy, N., Yashiro, S., Xie, H., Akiyama, S., Aguilar-Rodriguez, E., Kaiser, M.L., Howard, R.A., Bougeret, J.-L.: Astrophys. J. **674**, 560 (2008)
Harrison, R.A.: In: Gopalswamy, N., Mewaldt, R., Torsti, J. (eds.) Solar Eruptions and Energetic Particles. Geophysical Monograph Series, vol. 165, p. 73. American Geophysical Union, Washington DC (2006)
Howard, R.A., Michels, D.J., Sheeley, N.R. Jr., Koomen, M.J.: Astrophys. J. **263**, L101 (1982)
Hudson, H.S.: Solar Phys. **133**, 357 (1991)
Hundhausen, A.: In: Strong K.T., Saba J.L.R., Haisch B.M., Schmelz J.T. (eds.) The Many Faces of the Sun: A Summary of the Results from NASA's Solar Maximum Mission, p. 143. Springer, New York. (1999)
Kahler, S.W., Sheeley, N.R. Jr., Ligget, M.: Astrophys. J. **344**, 1026 (1989)
Kahler, S.W.: Ann. Rev. Astron. Astrophys. **30**, 113 (1992)
Kahler, S. W.: In: Gopalswamy, N., Mewaldt R., Torsti J.: (eds.) Solar Eruptions and Energetic Particles. Geophysical Monograph Series, vol. 165, p. 21. American Geophysical Union, Washington DC (2006)
Kay, H.R.M., Harra, L.K., Matthews, S.A., Culhane, J.L., Green, L.M.: Astron. Astrophys. **400**, 779 (2003)
Mann, G., Klassen, A., Aurass, H., Classen, H.-T.: Astron. Astrophys. **400**, 329 (2003)
Moon, Y.-J., Choe, G.S., Wang, H., Park, Y.D., Gopalswamy, N., Yang, G., Yashiro, S.: Astrophys. J. **581**, 694 (2002)
Munro, R.H., Gosling, J.T., Hildner, E., MacQueen, R.M., Poland, A.I., Ross, C.L., Solar Phys. **61**, 201 (1979)
Sheeley, N.R. Jr., Hakala, W.N, Wang, Y.-M.: J. Geophys. Res. **105**, 5081 (2000)
Song, P., Singer, H.J., Siscoe, G.L.: (eds.) Space Weather. Geophysical Monograph Series, vol. 125, p. 440. American Geophysical Union, Washington DC (2001)
St. Cyr, O.C., Webb, D.F., Solar Phys. **136**, 379 (1991).
Tylka, A., Lee, M.A.: Astrophys. J. **646**, 1319 (2006)
Vourlidas, A., Wu, S.T., Wang, A.H., Subramanian, P., Howard, R.A.: Astrophys. J. **598**, 1392 (2003)
Yashiro, S., Akiyama, S., Gopalswamy, N., Howard, R.A.: Astrophys. J. **650**, L143 (2006)
Yashiro, S., Michalek, G., Akiyama, S., Gopalswamy, N., Howard, R. A.: Astrophys. J. **673**, 1174 (2008)